Studies of granularity of a hadronic calorimeter for tens-of-TeV jets at a 100 TeV *pp* collider

S.V. Chekanov[a], A.V. Kotwal[b,c], J. Proudfoot[a], S. Sen[b], N.V. Tran[c], S.-S. Yu[e], Chih-Hsiang Yeh[e]

[a] *HEP Division, Argonne National Laboratory, 9700 S. Cass Avenue, Argonne, IL 60439, USA.*
[b] *Department of Physics, Duke University, USA*
[c] *Fermi National Accelerator Laboratory*
[d] *Department of Physics, Michigan State University, 220 Trowbridge Road, East Lansing, MI 48824*
[e] *Department of Physics, National Central University, Chung-Li, Taoyuan City 32001, Taiwan*

Abstract

Texts

Keywords: multi-TeV physics, *pp* collider, future hadron colliders, FCC, SppC

1. Introduction

Particle collisions at energies beyond those attained at the LHC will lead to many challenges for detector technologies. Future experiments, such as high-energy LHC (HE-LHC), future circular *pp* colliders of the European initiative, FCC-hh [1] and the Chinese initiative, SppC [2] will be required to measure high-momentum bosons (W, Z, H) and top quarks with strongly collimated decay products that form jets. Studies of jet substructure can help identify such particles.

The reconstruction of jet substructure variables for collimated jets with transverse momentum above 10 TeV require an appropriate detector design. The most important for reconstruction of such jets are tracking and calorimeter. Recently, a number of studies [3, 4, 5] have been discussed using various fast simulation tools, such as Delphes [6], in which momenta of particles are smeared to mimic detector response.

A major step towards the usage of full Geant4 simulation to verify the granularity requirements for calorimeters was made in [7]. The studies included in this paper have illustrated a significant impact of granularity of electromagnetic (ECAL) and hadronic (HCAL) calorimeters on the shape of hadronic showers calculated using calorimeter hits for two particles separated by some angle. It was concluded that high granularity is essential in resolving two close-by particles for energies above 100 GeV.

This paper makes another step in understanding understanding of this problem in terms of high-level physics quantities typically used in physics analyses. Similar to the studies presented in [7], this paper is based on full Geant4 simulation with realistic jet reconstruction.

2. Simulation of detector response and event reconstruction

The description of the detector and software used for this paper is discussed in [7]. We use the SiFCC detector geometry with a software package that represents a versatile environment for simulations of detector performance, testing new technology options, event reconstruction techniques for future 100 TeV colliders.

The GEANT4 (version 10.3) [8] simulation of calorimeter response was complemented with the full reconstruction of calorimeter clusters formed by the Pandora algorithm [9, 10]. Calorimeter clusters were built from calorimeter hits in the ECAL and HCAL after applying the corresponding sampling fractions. No other corrections are applied. Hadronic jets were reconstructed with the FASTJET package [11] using the anti-k_T algorithm [12] with a distance parameter of 0.5.

In the following discussion, we use the simulations of a heavy Z' boson, a hypothetical gauge boson that arises from extensions of the electroweak symmetry of the Standard Model. The Z' bosons were simulated with the masses, $M = 5$, 10, 20 and 40 TeV. The lowest value represents a typical mass that is within the reach of the LHC experiments. The value 40 TeV represents the physics reach of 100 TeV colliders. The Z' particles are forced to decay to to two light-flavor jets ($q\bar{q}$), W^+W^- or $t\bar{t}$, where W and t decay hadronically. In all such scenarios, two highly boosted jets are produced, which are typically back-to-back in the laboratory frame. Typical transverse momenta of such jets are $\simeq M/2$. The main difference between considered decay types lays in different jet substructure. In the case of the $q\bar{q}$ decays, jets do not have any internal structure. In the case of W^+W^-, each jet originates from W, thus it has two subjects because of the decay $W \rightarrow q\bar{q}$. In the case of hadronic top decays, jets have three subjects due to the decay $t \rightarrow W^+ b \rightarrow q\bar{q}b$ The signal events were generated using the PYTHIA8generator with the default settings, ignoring interference with SM processes. The event samples used in this paper are available from the HepSim database [13].

3. Studies of jet properties

First let us consider several variables that represent jet substructure using different types of calorimeter granularity. The question we want to answer is how close the reconstructed jet substructure variables to the input "truth" value that are reconstructed using input particles directly from the PYTHIA8generator.

The effective radius is the average of the energy weighted radial distance in $\eta - \phi$ space of jet constituents. Recently, it has been studied for multi-TeV jets in Ref.[14].

Let us study the effect of granularity on jet splitting scales. A jet k_T splitting scale [15] is defined as a distance measure used to form jets by the k_T recombination algorithm [16, 17]. This has been studied by ATLAS [18], and more recently in the context of 100 TeV physics [14]. The distribution of the splitting scale $\sqrt{d_{12}} = \min(p_T^1, p_T^2) \times \delta R_{12}$ [18] at the final stage of the k_T clustering, where two subjets are merged into the final one, is shown in Fig. 2.
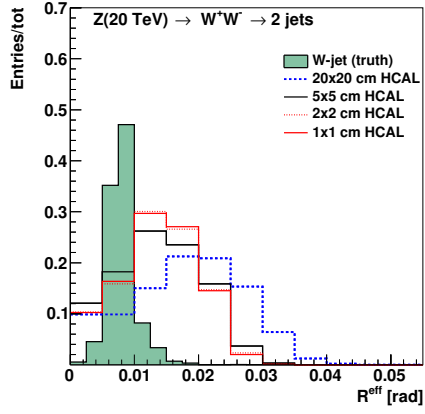
3.1. Jet subjettiness

We recall that N-subjettiness [? 19], τ_N, of jets has been proposed as a class of variables with which to study the decay products of a heavy particle inside jets. τ_N is
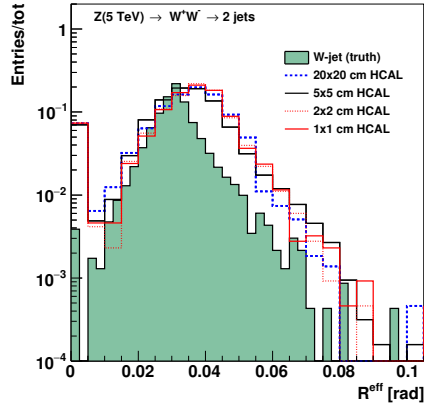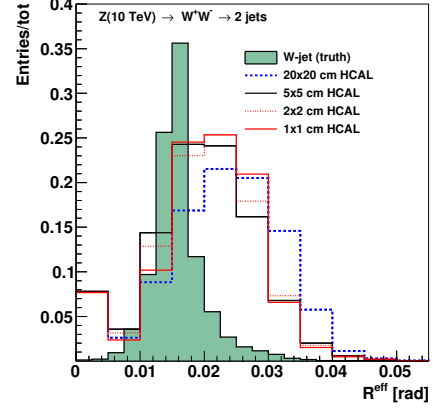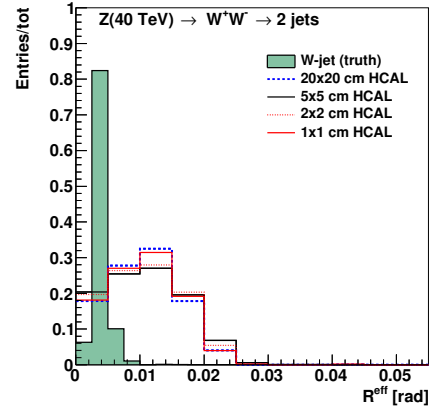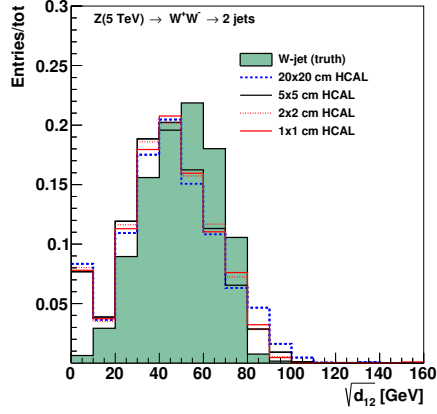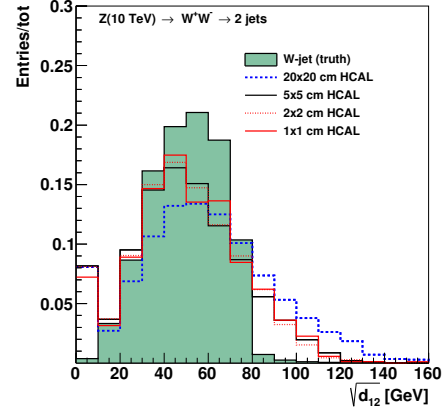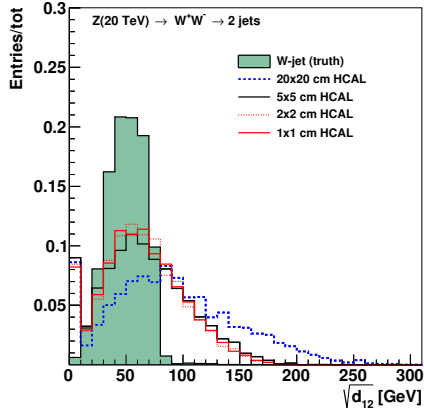
(a) 5 TeV

(b) 10 TeV

(c) 20 TeV

(d) 40 TeV

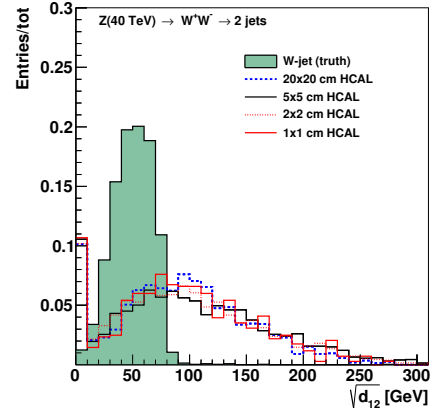Figure 1: Jet effective radius for different jet transverse moment and HCAL granularity.

(a) 5 TeV

(b) 10 TeV

(c) 20 TeV

(d) 40 TeV

Figure 2: Jet splitting scale for different jet transverse moment and HCAL granularity.

4

a measure of the degree to which a jet can be considered as being composed of N k_T-subjets [19]. The variable τ_{32}, defined as the ratio of the N-subjettiness variables τ_3/τ_2, is particularly sensitive to hadronically-decaying top-quark initiated jets. The variable, $\tau_{21} \equiv \tau_2/\tau_1$ can be used to reject background from W/Z decays. These variables do not strongly correlate with jet mass and can provide an independent check for the presence of top quarks. The jet substructure variables were obtained by re-running the k_T algorithm over the jet constituents of anti-k_T jets.

4. Soft drop method in future collider performance

In this section, we use the specific method about the soft-drop to study the performance of the detector in the different cell sizes. In the Figure , , , , are the distribution of the signal and background.

4.1. Analysis method

In this analysis, We fix the central at the median in signal distribution, and we use the different width to open the window to draw ROC curves.

4.2. The conclusion of the results

5. Studies of signal and background separation using Mann-Whitney U test and some new methods

(a) 5TeV at 20×20(cm×cm) in cluster

(b) 10TeV at 20×20(cm×cm) in cluster

(c) 20TeV at 20×20(cm×cm) in cluster

(d) 40TeV at 20×20(cm×cm) in cluster

(e) 5TeV at 5×5(cm×cm) in cluster

(f) 10TeV at 5×5(cm×cm) in cluster

(g) 20TeV at 5×5(cm×cm) in cluster

(h) 40TeV at 5×5(cm×cm) in cluster

(i) 5TeV at 1×1(cm×cm) in cluster

(j) 10TeV at 1×1(cm×cm) in cluster

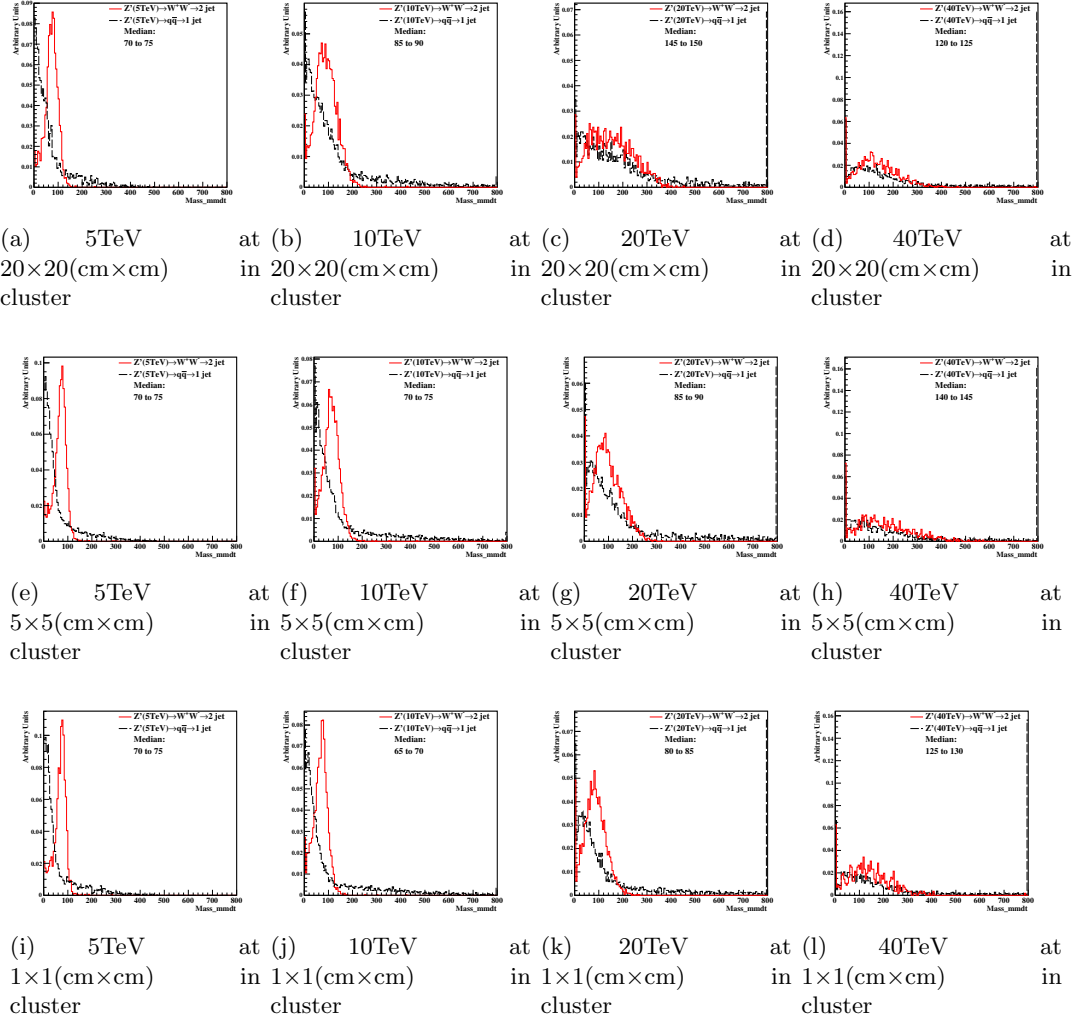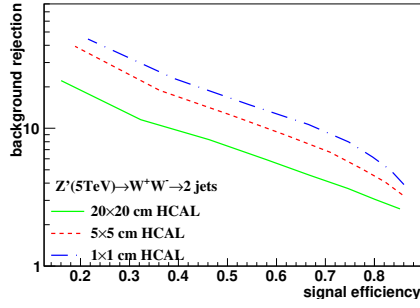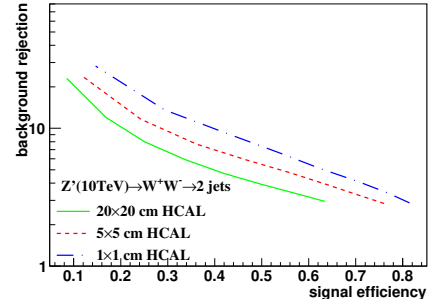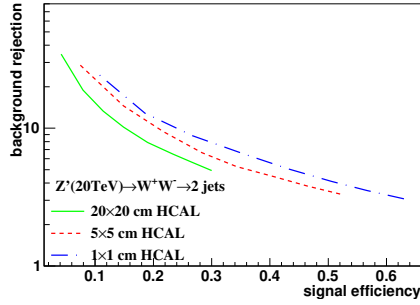(k) 20TeV at 1×1(cm×cm) in cluster

(l) 40TeV at 1×1(cm×cm) in cluster

Figure 3: Distributions of mass soft drop at β=0, signal=ww, in 5,10TeV energy of collision in different detector sizes. Cell Size in 20×20, 5×5, and 1×1(cm×cm) are shown here.
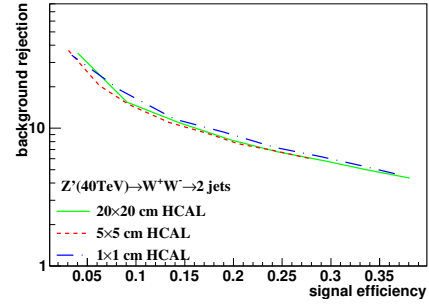
6

(a) Central at Median(20×20=,5×5=,1×1=) change width in cluster at 5TeV

(b) Central at Median(20×20=,5×5=,1×1=) change width in cluster at 10TeV

(c) Central at Median(20×20=,5×5=,1×1=) change width in cluster at 20TeV

(d) Central at Median(20×20=,5×5=,1×1=) change width in cluster at 40TeV

Figure 4: study of "fix central and change width" in mass soft drop at β=0, signal=ww, in 5, 10, 20, 40TeV energy of collision in different detector sizes. Cell Size in 20×20, 5×5, and 1×1(cm$\times$cm) are shown in each picture.

7

(a) 5TeV at 20×20(cm×cm) in cluster

(b) 10TeV at 20×20(cm×cm) in cluster

(c) 20TeV at 5×5(cm×cm) in cluster

(d) 40TeV at 5×5(cm×cm) in cluster

(e) 5TeV at 1×1(cm×cm) in cluster

(f) 10TeV at 1×1(cm×cm) in cluster

(g) 20TeV at 20×20(cm×cm) in cluster

(h) 40TeV at 20×20(cm×cm) in cluster

(i) 5TeV at 5×5(cm×cm) in cluster

(j) 10TeV at 5×5(cm×cm) in cluster

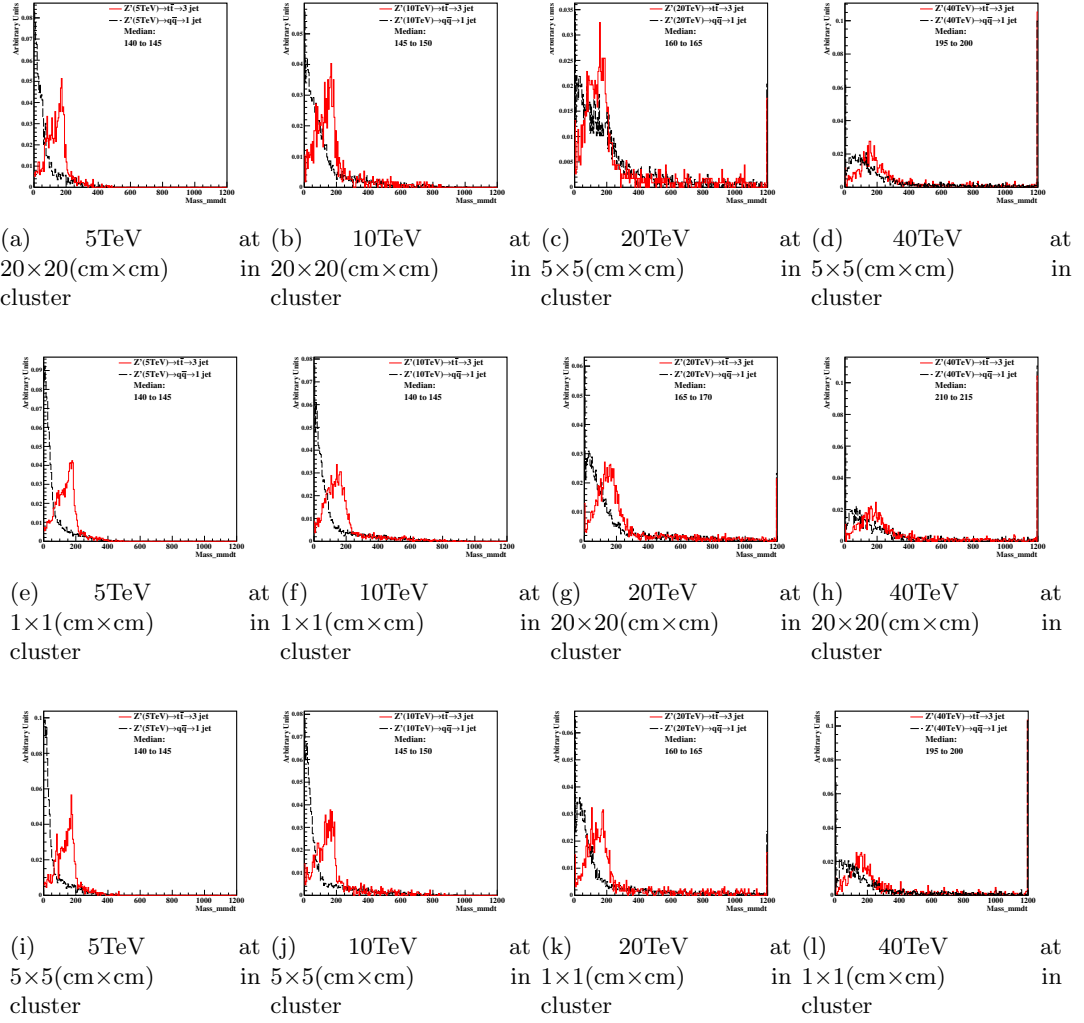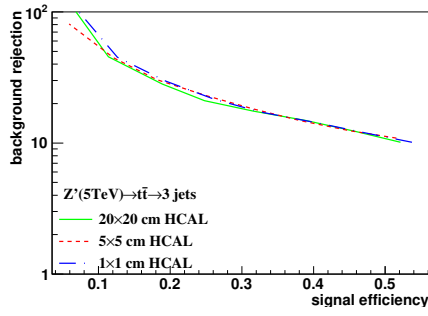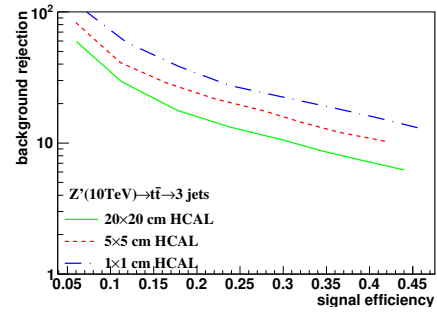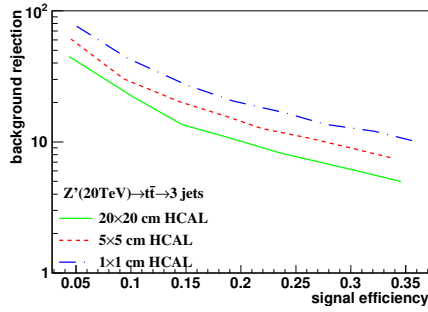(k) 20TeV at 1×1(cm×cm) in cluster

(l) 40TeV at 1×1(cm×cm) in cluster

Figure 5: Distributions of mass soft drop at β=0, signal=tt, in 5,10TeV energy of collision in different detector sizes. Cell Size in 20×20, 5×5, and 1×1(cm×cm) are shown here.
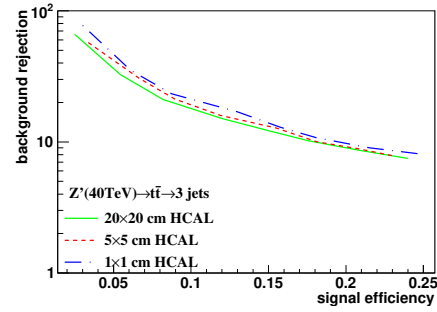
8

(a) Central at Median(20×20=,5×5=,1×1=) change width in cluster at 5TeV

(b) Central at Median(20×20=,5×5=,1×1=) change width in cluster at 10TeV

(c) Central at Median(20×20=,5×5=,1×1=) change width in cluster at 20TeV

(d) Central at Median(20×20=,5×5=,1×1=) change width in cluster at 40TeV

Figure 6: study of "fix central and change width" in mass soft drop at β=0, signal=tt, in 5, 10, 20, 40TeV energy of collision in different detector sizes. Cell Size in 20×20, 5×5, and 1×1(cm$\times$cm) are shown in each picture.

(a) 5TeV at 20×20(cm×cm) cluster

(b) 10TeV at in 20×20(cm×cm) cluster

(c) 20TeV at in 20×20(cm×cm) cluster

(d) 40TeV at in 20×20(cm×cm) cluster

(e) 5TeV at 5×5(cm×cm) cluster

(f) 10TeV at in 5×5(cm×cm) cluster

(g) 20TeV at in 5×5(cm×cm) cluster

(h) 40TeV at in 5×5(cm×cm) cluster

(i) 5TeV at 1×1(cm×cm) cluster

(j) 10TeV at in 1×1(cm×cm) cluster

(k) 20TeV at in 1×1(cm×cm) cluster
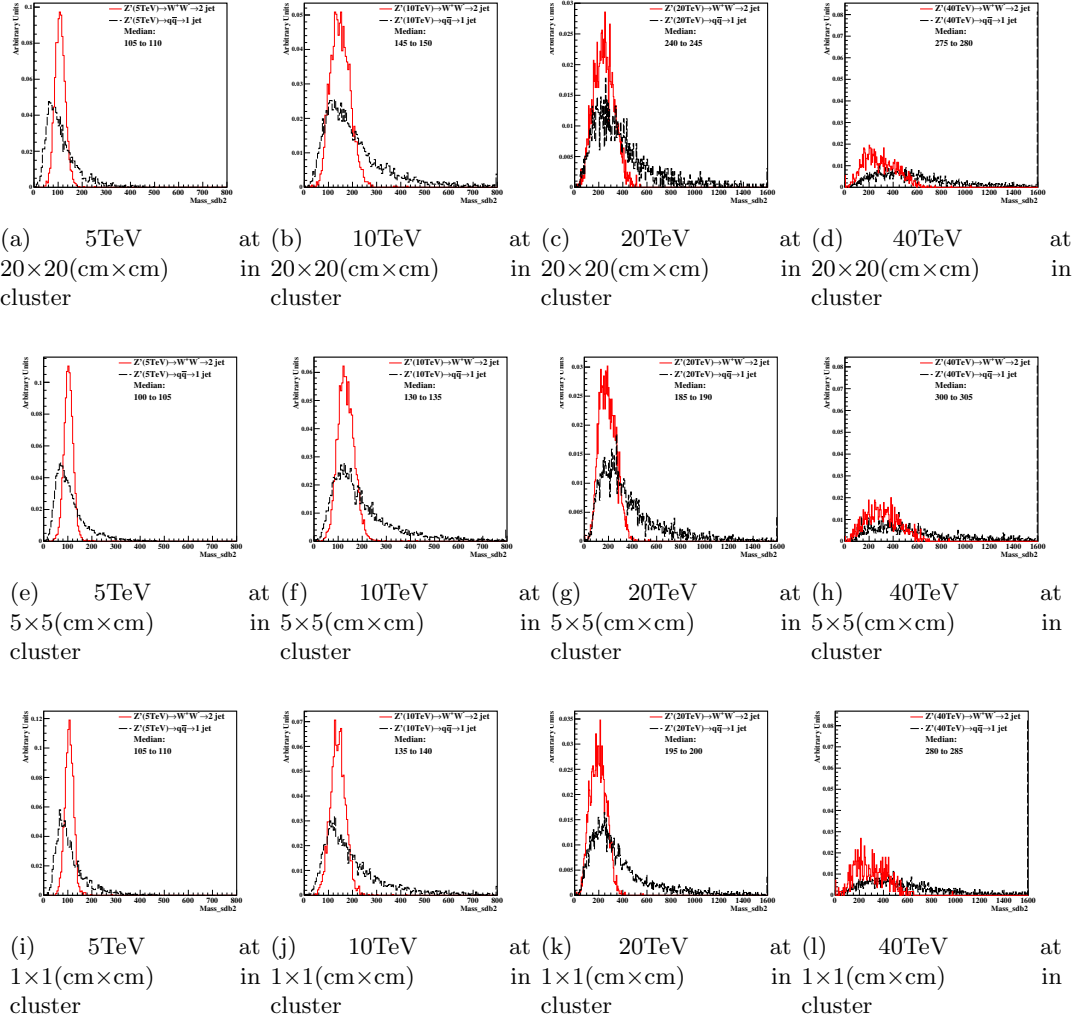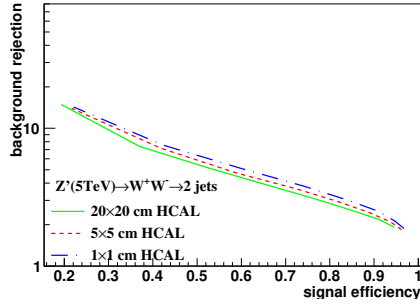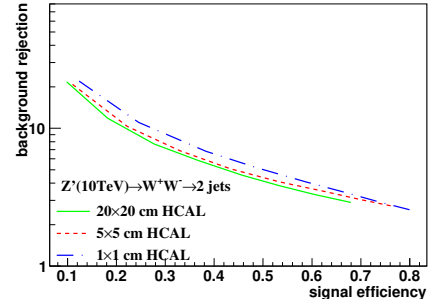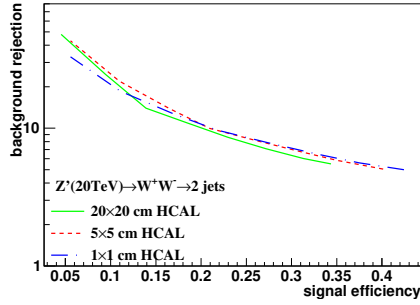
(l) 40TeV at in 1×1(cm×cm) cluster

Figure 7: Distributions of mass soft drop at β=2, signal=ww, in 5,10TeV energy of collision in different detector sizes. Cell Size in 20×20, 5×5, and 1×1(cm×cm) are shown here.
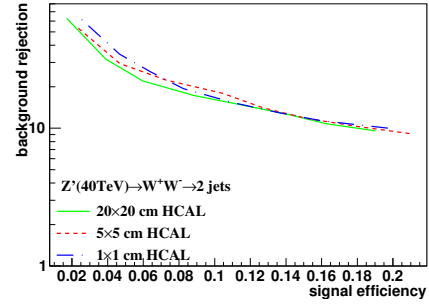
10

(a) Central at Median($20 \times 20 =$,$5 \times 5 =$,$1 \times 1 =$) change width in cluster at 5TeV

(b) Central at Median($20 \times 20 =$,$5 \times 5 =$,$1 \times 1 =$) change width in cluster at 10TeV

(c) Central at Median($20 \times 20 =$,$5 \times 5 =$,$1 \times 1 =$) change width in cluster at 20TeV

(d) Central at Median($20 \times 20 =$,$5 \times 5 =$,$1 \times 1 =$) change width in cluster at 40TeV

Figure 8: study of "fix central and change width" in mass soft drop at β=2, signal=ww, in 5, 10, 20, 40TeV energy of collision in different detector sizes. Cell Size in 20×20, 5×5, and 1×1(cm×cm) are shown in each picture.

(a)   5TeV   at 20×20(cm×cm) cluster

(b)   10TeV   at in 20×20(cm×cm) cluster

(c)   20TeV   at in 20×20(cm×cm) cluster

(d)   40TeV   at in 20×20(cm×cm) cluster

(e)   5TeV   at 5×5(cm×cm) cluster

(f)   10TeV   at in 5×5(cm×cm) cluster

(g)   20TeV   at in 5×5(cm×cm) cluster

(h)   40TeV   at in 5×5(cm×cm) cluster

(i)   5TeV   at 1×1(cm×cm) cluster

(j)   10TeV   at in 1×1(cm×cm) cluster

(k)   20TeV   at in 1×1(cm×cm) cluster

(l)   40TeV   at in 1×1(cm×cm) cluster

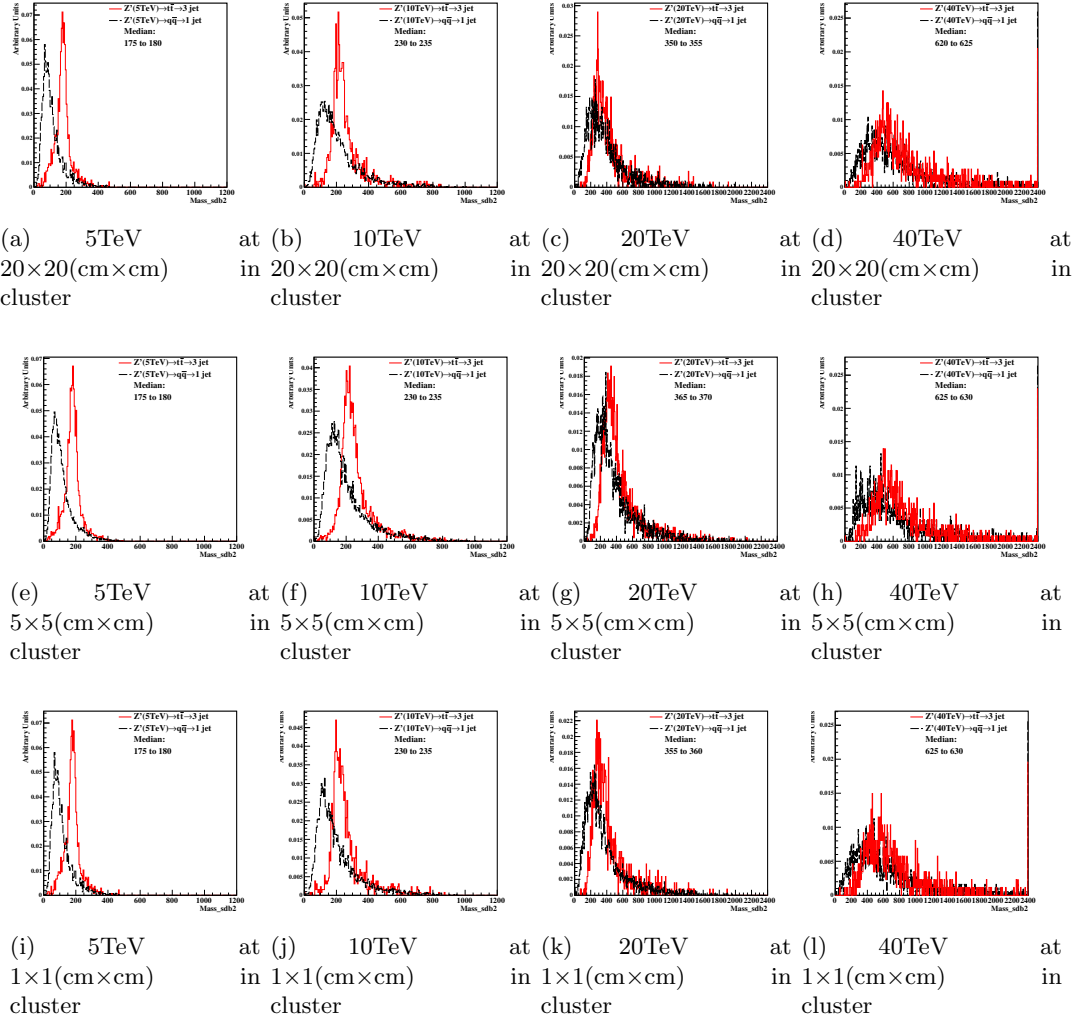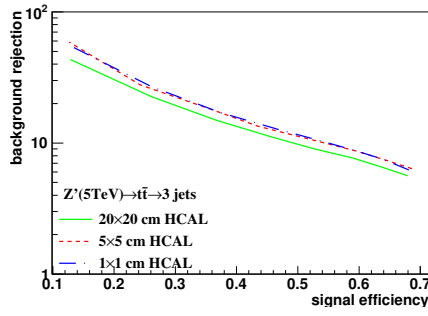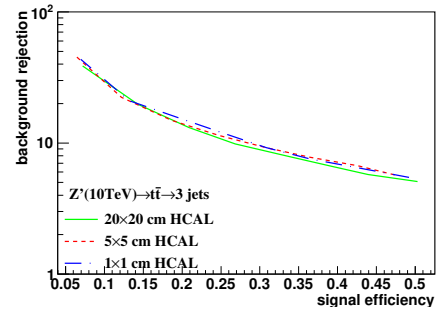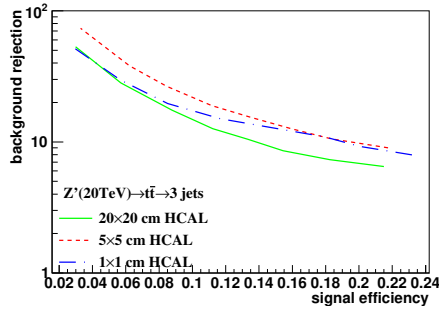Figure 9: Distributions of mass soft drop at β=2, signal=tt, in 5,10TeV energy of collision in different detector sizes. Cell Size in 20×20, 5×5, and 1×1(cm×cm) are shown here.

12

(a) Central at Median($20 \times 20=,5 \times 5=,1 \times 1=$) change width in cluster at 5TeV

(b) Central at Median($20 \times 20=,5 \times 5=,1 \times 1=$) change width in cluster at 10TeV
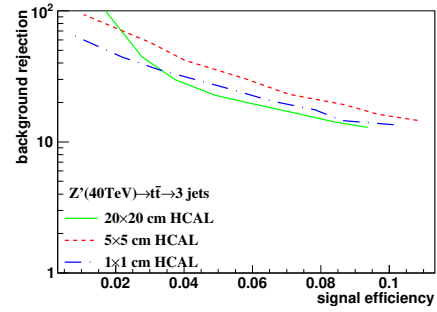
(c) Central at Median($20 \times 20=,5 \times 5=,1 \times 1=$) change width in cluster at 20TeV

(d) Central at Median($20 \times 20=,5 \times 5=,1 \times 1=$) change width in cluster at 40TeV

Figure 10: study of "fix central and change width" in mass soft drop at $\beta=2$, signal=tt, in 5, 10, 20, 40TeV energy of collision in different detector sizes. Cell Size in 20×20, 5×5, and 1×1(cm×cm) are shown in each picture.

(a) 5TeV at 20×20(cm×cm) 0.5GeV

(b) 10TeV at in 20×20(cm×cm) 0.5GeV

(c) 20TeV at in 20×20(cm×cm) 0.5GeV

(d) 40TeV at in 20×20(cm×cm) in 0.5GeV

(e) 5TeV at 5×5(cm×cm) 0.5GeV

(f) 10TeV at in 5×5(cm×cm) 0.5GeV

(g) 20TeV at in 5×5(cm×cm) 0.5GeV

(h) 40TeV at in 5×5(cm×cm) in 0.5GeV

(i) 5TeV at 1×1(cm×cm) 0.5GeV

(j) 10TeV at in 1×1(cm×cm) 0.5GeV

(k) 20TeV at in 1×1(cm×cm) 0.5GeV
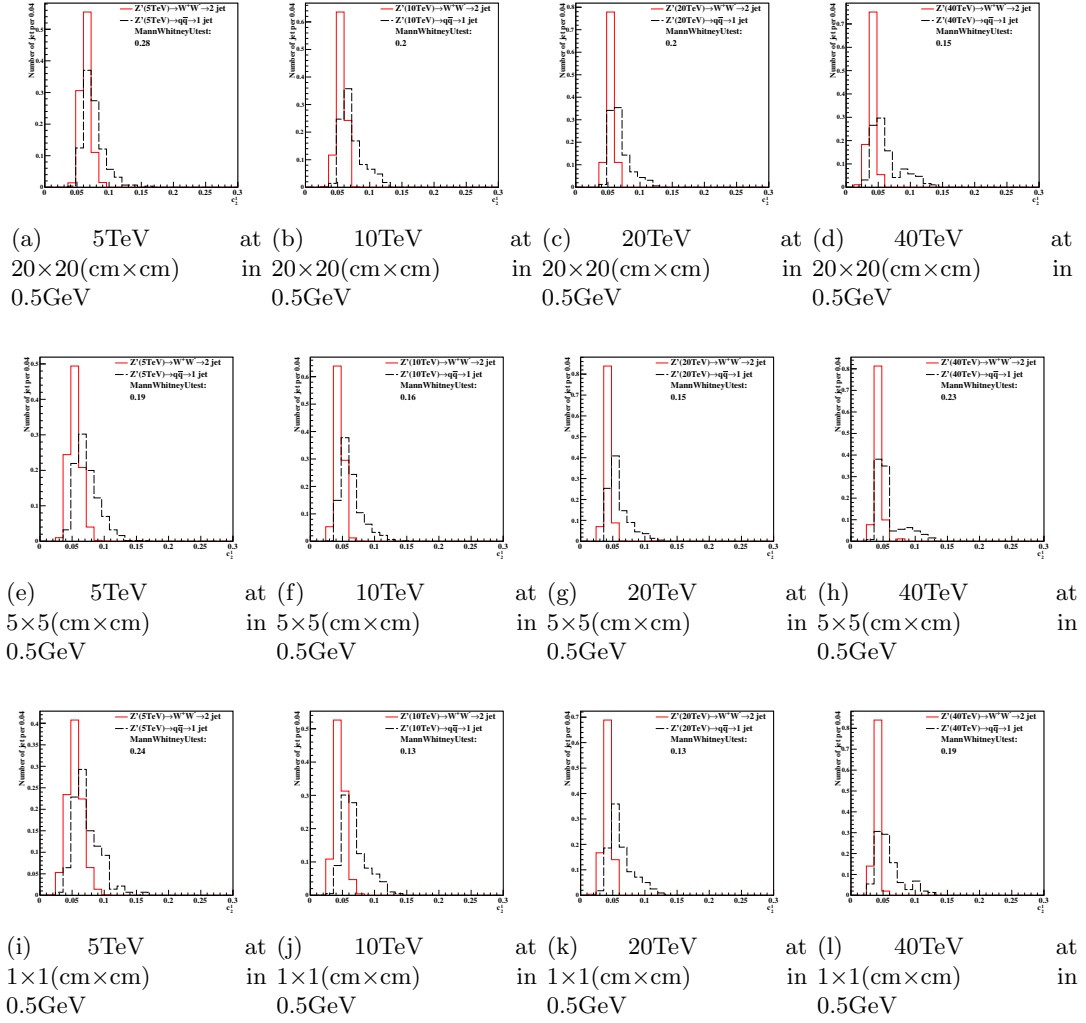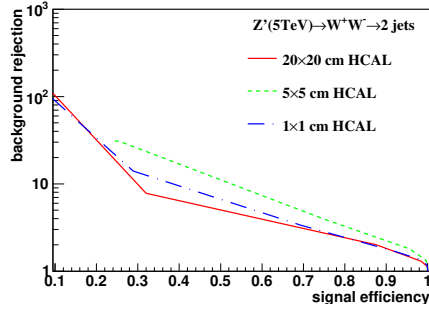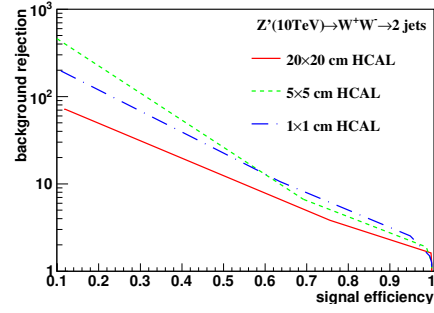
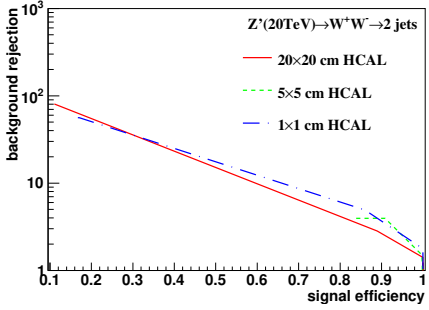(l) 40TeV at in 1×1(cm×cm) in 0.5GeV

Figure 11: Distributions of Mann-Whitney value U in 5, 10, 20, 40TeV energy collision for c2b1 in different detector sizes. Cell Size in 20×20, 5×5, and 1×1(cm×cm) are shown here.
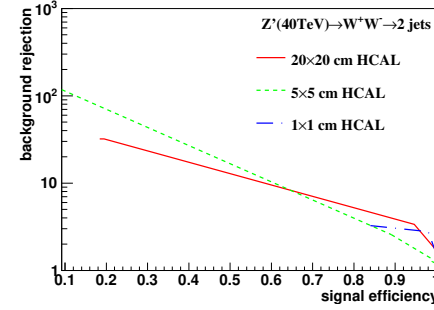
14

(a) 5 TeV using Rawhit 0.5GeV cut method with New2 after cut Method

(b) 10 TeV using Rawhit 0.5GeV cut method with New2 after cut Method

(c) 20 TeV using Rawhit 0.5GeV cut method with New2 after cut Method

(d) 40 TeV using Rawhit 0.5GeV cut method with New2 after cut Method

Figure 12: Signal efficiency versus background rejection rate using c2b1.The energies of collision at (a)5, (b)10, (c)20, (d)40TeV are shown here. In each picture, the three ROC curves correspond to different detector sizes.

(a) 5TeV at 20×20(cm×cm) in 0.5GeV

(b) 10TeV at 20×20(cm×cm) in 0.5GeV

(c) 20TeV at 20×20(cm×cm) in 0.5GeV

(d) 40TeV at 20×20(cm×cm) in 0.5GeV

(e) 5TeV at 5×5(cm×cm) in 0.5GeV

(f) 10TeV at 5×5(cm×cm) in 0.5GeV

(g) 20TeV at 5×5(cm×cm) in 0.5GeV

(h) 40TeV at 5×5(cm×cm) in 0.5GeV

(i) 5TeV at 1×1(cm×cm) in 0.5GeV

(j) 10TeV at 1×1(cm×cm) in 0.5GeV

(k) 20TeV at 1×1(cm×cm) in 0.5GeV
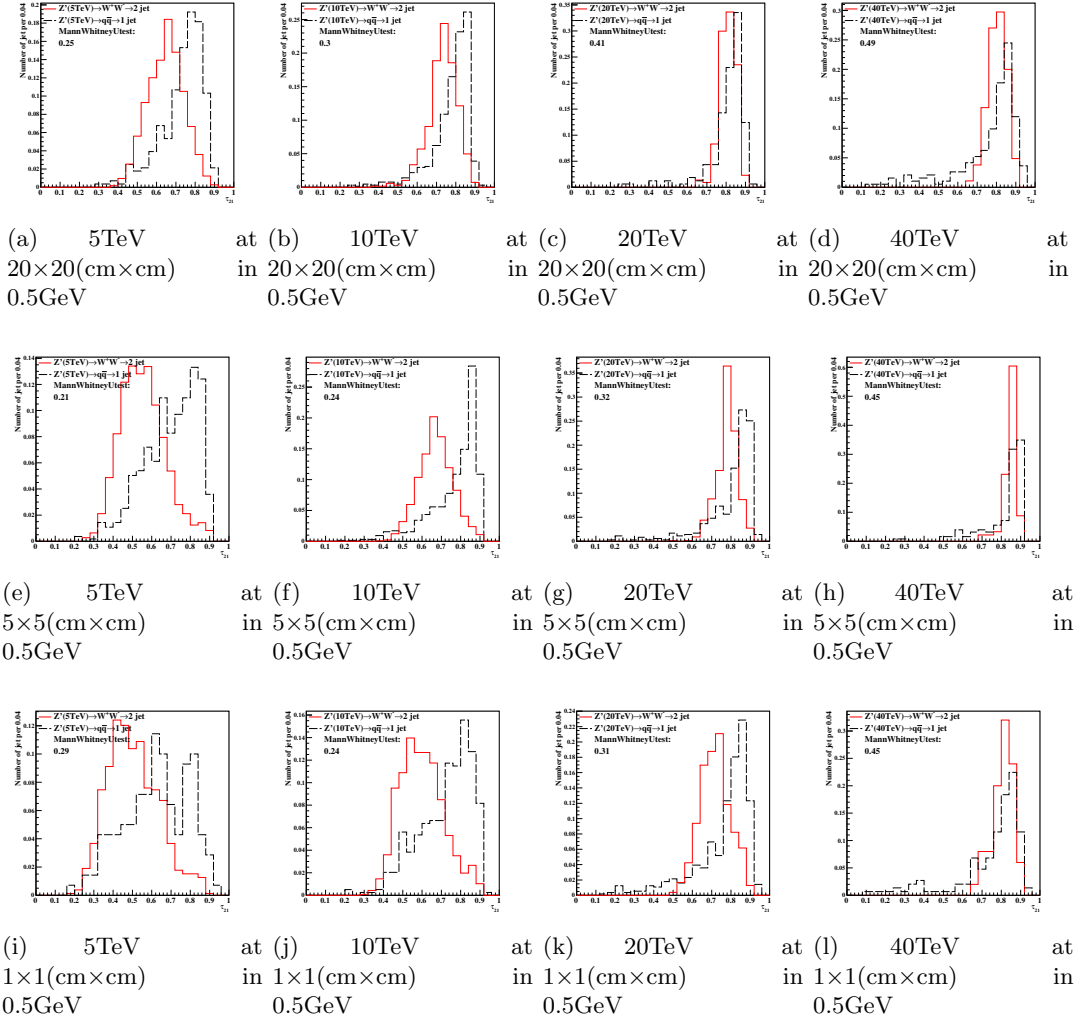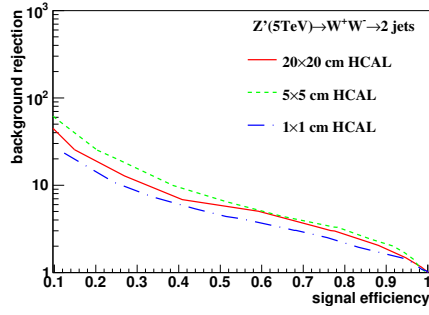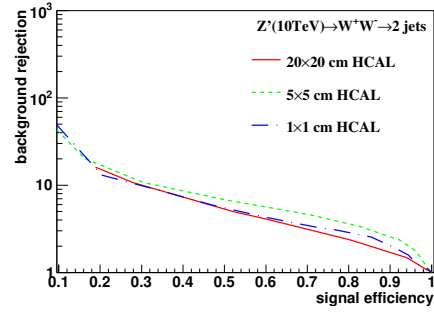
(l) 40TeV at 1×1(cm×cm) in 0.5GeV

Figure 13: Distributions of Mann-Whitney value U in 5, 10, 20, 40TeV energy collision for τ_{21} in different detector sizes. Cell Size in 20×20, 5×5, and 1×1(cm×cm) are shown here.

16

(a) 5 TeV using Rawhit 0.5GeV cut method with New2 after cut Method

(b) 10 TeV using Rawhit 0.5GeV cut method with New2 after cut Method

(c) 20 TeV using Rawhit 0.5GeV cut method with New2 after cut Method

(d) 40 TeV using Rawhit 0.5GeV cut method with New2 after cut Method

Figure 14: Signal efficiency versus background rejection rate using τ_{21}. The energies of collision at (a)5, (b)10, (c)20, (d)40TeV are shown here. In each picture, the three ROC curves correspond to different detector sizes.
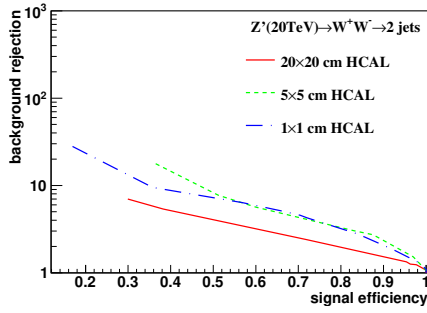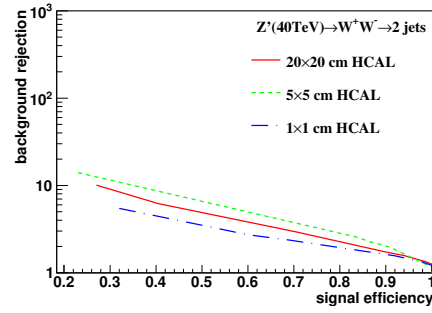
(a)   5TeV   at
20×20(cm×cm)
0.5GeV

(b)   10TeV   at
in 20×20(cm×cm)
0.5GeV

(c)   20TeV   at
in 20×20(cm×cm)
0.5GeV

(d)   40TeV   at
in 20×20(cm×cm)   in
0.5GeV

(e)   5TeV   at
5×5(cm×cm)
0.5GeV

(f)   10TeV   at
in 5×5(cm×cm)
0.5GeV

(g)   20TeV   at
in 5×5(cm×cm)
0.5GeV

(h)   40TeV   at
in 5×5(cm×cm)   in
0.5GeV

(i)   5TeV   at
1×1(cm×cm)
0.5GeV

(j)   10TeV   at
in 1×1(cm×cm)
0.5GeV

(k)   20TeV   at
in 1×1(cm×cm)
0.5GeV

(l)   40TeV   at
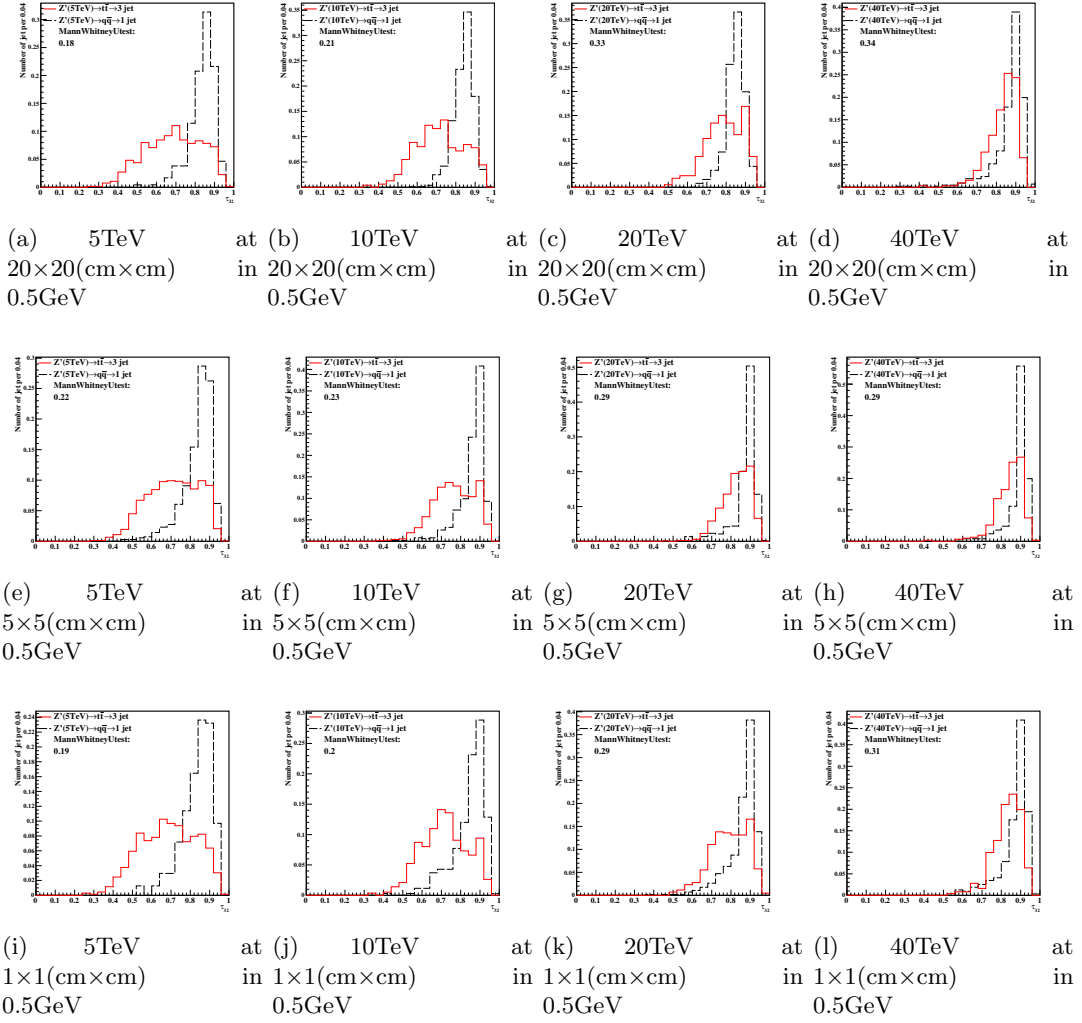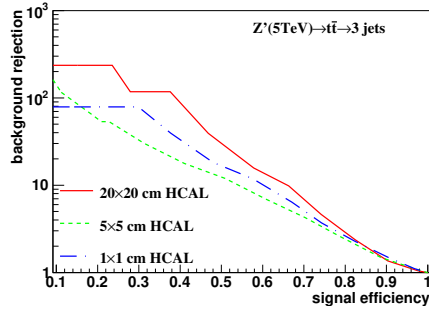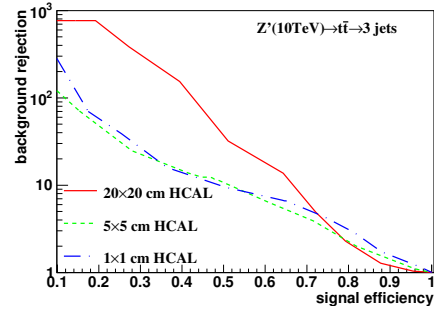in 1×1(cm×cm)   in
0.5GeV

Figure 15: Distributions of Mann-Whitney value U in 5, 10, 20, 40TeV energy collision for τ_{32} in different detector sizes. Cell Size in 20×20, 5×5, and 1×1(cm×cm) are shown here.

18

(a) 5 TeV using Rawhit 0.5GeV cut method with New2 after cut Method

(b) 10 TeV using Rawhit 0.5GeV cut method with New2 after cut Method

(c) 20 TeV using Rawhit 0.5GeV cut method with New2 after cut Method

(d) 40 TeV using Rawhit 0.5GeV cut method with New2 after cut Method

Figure 16: Signal efficiency versus background rejection rate using τ_{32}. The energies of collision at (a)5, (b)10, (c)20, (d)40TeV are shown here. In each picture, the three ROC curves correspond to different detector sizes.
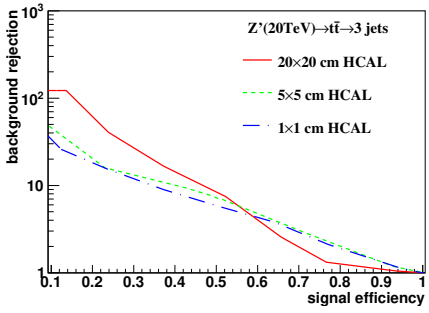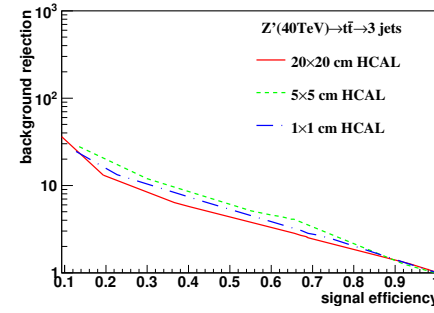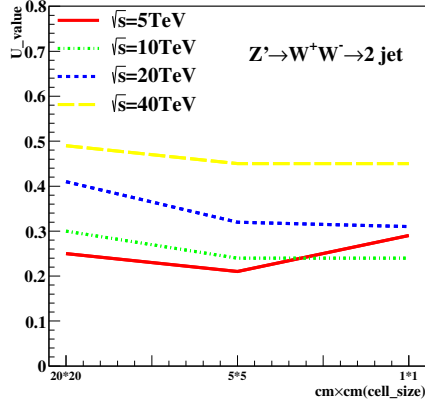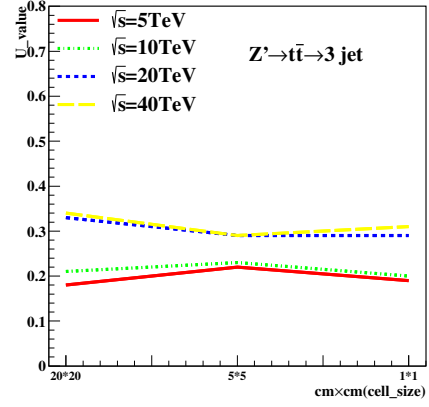
19

(a) τ_{21} rawhit cut at 0.5GeV

(b) τ_{32} rawhit cut at 0.5GeV
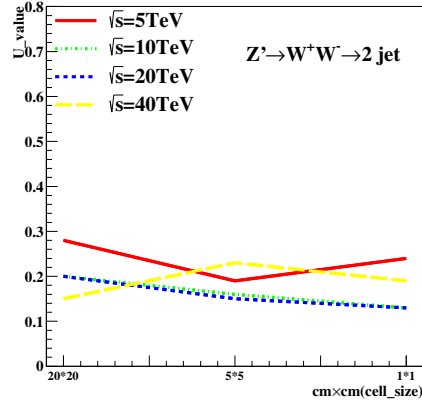
(c) $c_2^{(1)}$ rawhit cut at 0.5GeV

Figure 17: The Mann-Whitney U values for τ_{21}, τ_{32} and $c_2^{(1)}$ reconstructed from calorimeter hit at 05GeV cut at different collision energies correspond to different detector sizes in rawhit cut at 05GeV. The energies of collision at 5, 10, 20, 40, 20, 40TeV are shown in each figure.

References

[1] M. Benedikt, The Global Future Circular Colliders EffortCERN-ACC-SLIDES-2016-0016. Presented at P5 Workshop on the Future of High Energy Physics, BNL, USA, Dec. 15-18, 2013.
URL http://cds.cern.ch/record/2206376

[2] J. Tang, et al., Concept for a Future Super Proton-Proton Collider (2015). arXiv:1507.03224.

[3] R. Calkins, et al., Reconstructing top quarks at the upgraded LHC and at future accelerators, in: Proceedings, Community Summer Study 2013: Snowmass on the Mississippi (CSS2013): Minneapolis, MN, USA, July 29-August 6, 2013. arXiv:1307.6908.
URL https://inspirehep.net/record/1244676/files/arXiv:1307.6908.pdf

[4] S. V. Chekanov, J. Dull, Energy range of hadronic calorimeter towers and cells for high-pT jets at a 100 TeV colliderarXiv:1511.01468.

[5] E. Coleman, M. Freytsis, A. Hinzmann, M. Narain, J. Thaler, N. Tran, C. Vernieri, The importance of calorimetry for highly-boosted jet substructurearXiv:1709.08705.

[6] DELPHES 3 Collaboration, J. de Favereau, C. Delaere, P. Demin, A. Giammanco, V. Lematre, A. Mertens, M. Selvaggi, DELPHES 3, A modular framework for fast simulation of a generic collider experiment, JHEP 02 (2014) 057. arXiv:1307.6346, doi:10.1007/JHEP02(2014)057.

[7] S. V. Chekanov, M. Beydler, A. V. Kotwal, L. Gray, S. Sen, N. V. Tran, S. S. Yu, J. Zuzelski, Initial performance studies of a general-purpose detector for multi-TeV physics at a 100 TeV pp collider, JINST 12 (06) (2017) P06009. arXiv:1612.07291, doi:10.1088/1748-0221/12/06/P06009.

[8] J. Allison, et al., Recent developments in Geant4, Nuclear Instruments and Methods in Physics Research A 835 (2016) 186.

[9] M. J. Charles, PFA Performance for SiD, in: Linear colliders. Proceedings, International Linear Collider Workshop, LCWS08, and International Linear Collider Meeting, ILC08, Chicago, USA, Novermber 16-20, 2008 , 2009. arXiv:0901.4670.

[10] J. S. Marshall, M. A. Thomson, Pandora Particle Flow Algorithm, in: Proceedings, International Conference on Calorimetry for the High Energy Frontier (CHEF 2013), 2013, pp. 305–315. arXiv:1308.4537.

[11] G. P. S. M. Cacciari, G. Soyez, FastJet user manual CERN-PH-TH/2011-297. arXiv:1111.6097.

[12] M. Cacciari, G. P. Salam, G. Soyez, The anti-kt jet clustering algorithm, JHEP 0804 (2008) 063. arXiv:0802.1189.

[13] S. Chekanov, HepSim: a repository with predictions for high-energy physics experiments, Advances in High Energy Physics 2015 (2015) 136093, available as http://atlaswww.hep.anl.gov/hepsim/.

[14] B. Auerbach, S. Chekanov, J. Love, J. Proudfoot, A. Kotwal, Sensitivity to new high-mass states decaying to ttbar at a 100 TeV collider arXiv:1412.5951.

[15] J. Butterworth, B. Cox, J. R. Forshaw, WW scattering at the CERN LHC, Phys.Rev. D65 (2002) 096014. arXiv:hep-ph/0201098, doi:10.1103/PhysRevD.65.096014.

[16] S. Catani, Y. L. Dokshitzer, M. H. Seymour, B. R. Webber, Longitudinally-invariant k-clustering algorithms for hadron-hadron collisions, Nuclear Physics B 406 (12) (1993) 187 – 224.
URL http://www.sciencedirect.com/science/article/pii/055032139390166M

[17] S. D. Ellis, D. E. Soper, Successive combination jet algorithm for hadron collisions, Phys. Rev. D48 (1993) 3160–3166. arXiv:hep-ph/9305266, doi:10.1103/PhysRevD.48.3160.

[18] ATLAS Collaboration Collaboration, G. Aad, et al., Jet mass and substructure of inclusive jets in $\sqrt{s} = 7$ TeV pp collisions with the ATLAS experiment, JHEP 1205 (2012) 128. arXiv:1203.4606, doi:10.1007/JHEP05(2012)128.

[19] J. Thaler, K. Van Tilburg, Identifying Boosted Objects with N-subjettiness, JHEP 03 (2011) 015. arXiv:1011.2268, doi:10.1007/JHEP03(2011)015.